Performance of UV and IR Sensors for Inspections of Power Equipment

G. Komar[1], O. Pischler[1], U. Schichler[1] & R.-L. Vieriu[2]
[1]*Institute of High Voltage Engineering and System Performance, Graz University of Technology, Graz, Austria*
[2]*SIEMENS AG Österreich, Corporate Technology, Active Vision Technologies, Graz, Austria*
gernot.komar@tugraz.at

Abstract

Electric power infrastructure, such as transmission lines or substations, is usually routinely inspected to assess its condition. The vast majority of typical defects in power transmission equipment manifests itself either through corona phenomena or through thermal effects. Therefore, an IR camera and a solar blind UV camera are sufficient for the detection of most defects in power transmission equipment. In the past, many network operators have relied mostly on manual inspections. In recent years, however, manned as well as unmanned aerial inspection methods, which are significantly more time effective, have become increasingly affordable and are therefore gaining in popularity rapidly.

To obtain meaningful measurement results, many factors must be taken into account, which can even be difficult with conventional, static measurements. In the case of highly dynamic measurement practices (airborne or vehicle based), the combination of velocity and distance presents further challenges.

This contribution is focused on the detection performance of UV and IR sensors under dynamic conditions. For this purpose, experiments were carried out with a typical IR and UV/corona camera at various distances to artificial defects. Additionally, a method for the automatic evaluation of UV und IR data based on machine learning is presented.

1. Introduction

To ascertain the highest possible security of supply, network operators routinely inspect their infrastructure. Many network operators use manual inspections, carried out by specialized personnel, for this purpose. Fortunately, the vast majority of typical defects in power transmission equipment manifests itself either through corona phenomena or through thermal effects. Therefore, an IR camera and a solar blind UV camera are sufficient for the detection of most defects in power transmission equipment. However, varying geographical conditions and frequent needs for follow-up inspections make those procedures rather time and staff intensive. As a result, manned as well as unmanned aerial inspection methods, which became increasingly affordable in recent years and are in general more time effective, are gaining in popularity rapidly.

In order to obtain meaningful measurement results, many factors must be taken into account, which can even be difficult with conventional, static measurements.

In the case of dynamic measurement practices, the combination of velocity and distance presents further challenges. So far, there are no comprehensive standards or guidelines for UV and IR which adequately cover the special conditions that dynamic measurement methods imply.

In this contribution an attempt is made to determine conditions under which a qualitatively meaningful fault detection and evaluation is possible and useful. Particular attention is paid to assess the influence velocity and distance have on the detection sensitivity as well as the detection accuracy. For this purpose, results from measurements performed on selected laboratory and outdoor fault scenarios at various distances and velocities using an automated turntable are presented (Figure 1).
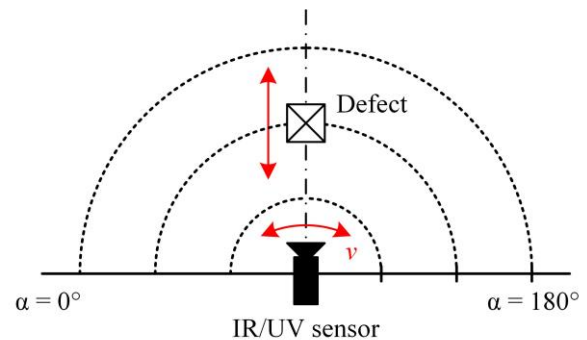

Figure 1. Setup for dynamic UV and IR measurements at various velocities and distances

2. Performance of IR sensors in dynamic use

2.1 State-of-the-art

Primarily, IR sensors are used for local testing of electrical power equipment. In order to determine the temperature as accurately as possible, some environmental aspects, in addition to a suitable camera, must be taken into account. This includes variables such as the surface condition and the current load of the object, but also ambient temperature, wind velocity, sky as well as solar radiation and cloudage. All of those parameters also play a significant role when IR sensors are used for dynamic measurements. Additionally, the relative velocity and distance to the test object must be taken into account. In this chapter experimental results will be presented to investigate the influence of velocity and distance on the measurement results. In order to avoid influences of weather phenomena and reflected solar radiation, the experiments were carried out indoors.

2.2 IR sensor

In earlier tests, the Optris PI640 was selected for the experiments on a moving device. Preliminary laboratory tests have shown that actively cooled cameras may have slightly better performances under dynamic conditions. However, the selected camera provides the best overall package in terms of its characteristics, its weight and its digital interfaces. Especially the last two attributes are very important for future use on autonomous, moveable devices. The key facts of this camera are shown in Table 1.

Table 1. Technical details of the Optris PI640

Detector	FPA, uncooled (17 µm x 17 µm)
Optical resolution	640 x 480 pixel
Spectral range	7.5 – 13 µm
Temperature ranges	0 °C...250 °C
Frame rate	32 Hz
Thermal sensitivity	75 mK
Ambient temperature	0 °C...70 °C
Enclosure (size / rating)	46 mm x 56 mm x 90 mm / IP 67

2.3 Testing environment

The test object was a conductor loop of 10 m length whose ends were jointed with a suitable cable clamp. The conductor cable has a diameter of 21 mm and a glass bead-blasted surface. The emission coefficient is given by the manufacturer as $\varepsilon = 0.6$. The clamp is made out of cast aluminium and consists of two parts that are fixed with one screw on each side (Figure 2). The emission coefficient for the clamp was assumed to be $\varepsilon = 0.4$ according to previous measurements.

Figure 2. Clamp with bead-blasted conductors

The loop was passed through an AC current transformer and loaded with an initial current of 300 A which was adjusted in order to obtain the desired temperatures. To measure the temperature, five thermocouples were fitted, two on the clamp (1x front / 1x back) and three on the conductor (Figure 2). The temperatures were recorded during the whole process, from heating up until 30 minutes after the last measurement. The temperatures of the clamp during the recording of the thermograms were obtained by linear interpolation.

The clamp was loosened to attain a temperature difference between rope and clamp of about 10 K at a clamp temperature of about 60 °C. This value can be taken as a benchmark for a minimal alert temperature difference in detecting hot-spots [1, 2]. After reaching stationary temperatures, measurements were taken at three different distances (10 m, 20 m and 30 m).

For every distance the velocity was varied in following steps: 0 m/s (static), 2 m/s, 5 m/s, 7 m/s and 10 m/s. To ensure reproducible relative velocities between the IR camera and the test object, the camera was mounted on an automated turntable which was controlled by a stepper motor and a microcontroller (Figure 1). For every step the IR temperature was obtained for the clamp and two spots on the conductor (Table 2). The emission coefficient was fixed for the whole camera range. In this case, the influence of three different emission coefficients ($\varepsilon = 1$, 0.6, 0.4) were explored. As result, IR-sequences were recorded for every performed measurement.

Table 2. Average temperatures during measurement process

Location	Average temperature in °C		
	10 m	20 m	30 m
S1 (clamp)	57,7	58,6	58,5
S2 (clamp)	58,6	59,5	59,8
S3 (conductor)	48,9	50,1	50,5
S4 (conductor)	47,1	46,1	45,3
S5 (conductor)	49,6	48,2	47,6
Ambient	20,5	20,3	20,0

Out of those thermograms, temperature values were obtained from three predefined areas (Figure 3). To compare the temperatures for every distance in a reproducible way, the maximum temperature values were recorded from every area. Also, the IR temperatures are given in relation to the temperatures measured on the surface.
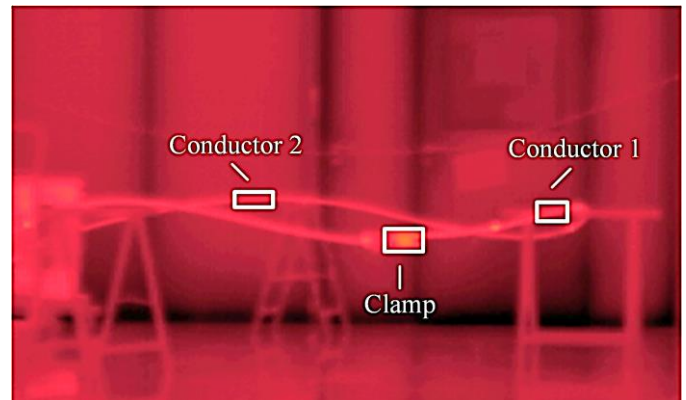
Figure 3. Measuring areas for the IR temperatures

2.4 Results

When looking at the graphs in Figures 4 and 5 it is recognizable, that the detected temperatures depend on camera velocity and distance. For an estimated emission coefficient of $\varepsilon = 1$ the IR sensor only detects 64 % to 42 % of the origin clamp temperatures, depending on velocity and distance. The influence of the sensor velocity gets smaller with increasing distance.

As far as the conductor is concerned, the influences of speed and distance on the observed temperature are almost negligible. The detection efficiency is about the same as for the clamp (Figures 4 and 5).

In case of the clamp, the influencing effects become much more obvious. The recorded results show that the basic course of every curve is nearly the same. Furthermore, the comparison of the different curves indicates that the closer the emission coefficient of the clamp gets towards to the actual value, the closer the temperatures approach the values determined in situ with the thermo-couples (Figures 5 and 6). Looking at the variations between different curves for different distances, it is recognizable, that lower emission coefficients cause a higher dependency on the distance of the sensor (Figures 5 – 7). The results indicate, that the influence of the sensor velocity is getting smaller with longer distances between sensor and object. The same effect is achieved if the emission coefficient is set to a higher value (Table 3).
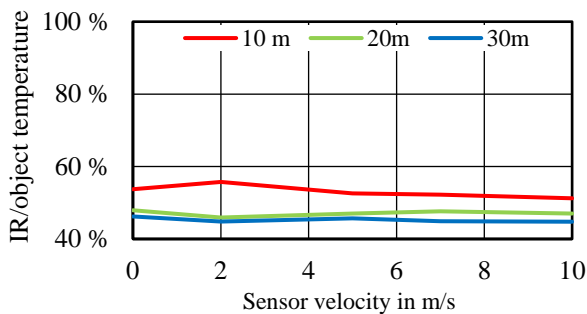
Table 3. Temperature difference between 0 and 10 m/s

Distance	Temperature difference in %		
	ε = 1	ε = 0.6	ε = 0.4
10 m	10,4	16,4	22,7
20 m	5,7	9,1	12,6
30 m	3,3	5,1	7,0

In summary it can be stated, that in this experiment the detected temperatures were more constant when a higher emission coefficient was used. However, higher emission coefficients also led to less accurate temperature measurements.

Regarding the influence of different sensor velocities on the temperature difference ΔT between the clamp and the conductor the sensor velocity appears to have less influence at higher distances, but the detection efficiency is then already lower than 50 % of the original ΔT value (Figure 8). Increasing the distance between sensor and object leads to a similar behavior. However, this behavior is desirable because the minimum distances, which must be kept between the infrastructure and inspection equipment, usually exceeds 30 m. The investigations regarding the temperature differences ΔT show that lower values for the emission coefficient deliver results that are closer to the actual temperature difference (Figure 9).

Figure 4. Conductor temperatures with ε = 1
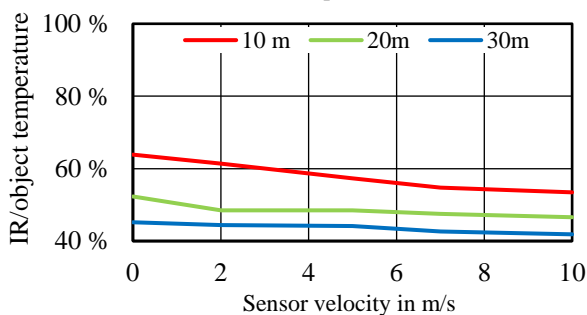
Figure 5. Clamp temperatures with ε = 1
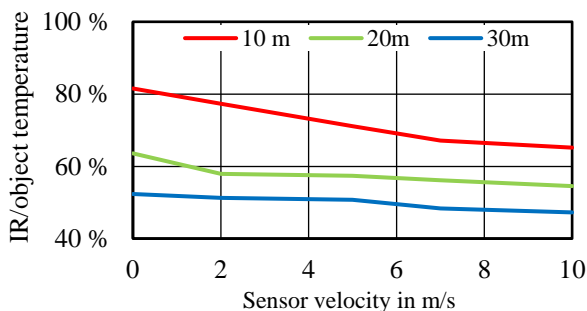
Figure 6. Clamp temperatures with ε = 0.6
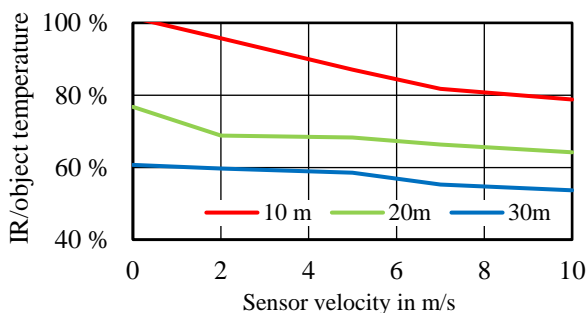
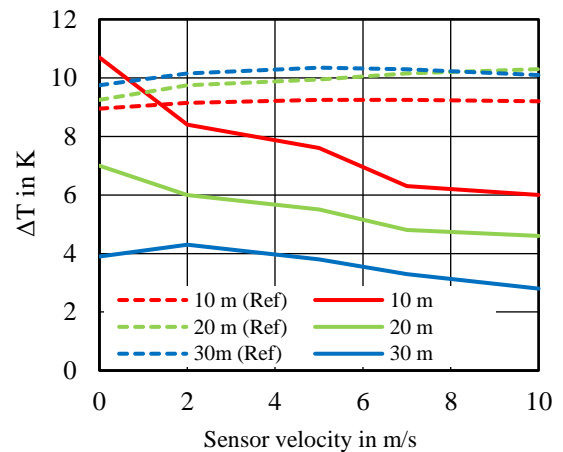**Figure 7.** Clamp temperatures with ε = 0.4

Figure 8. IR detected temperature differences between clamp and conductor with ε = 1
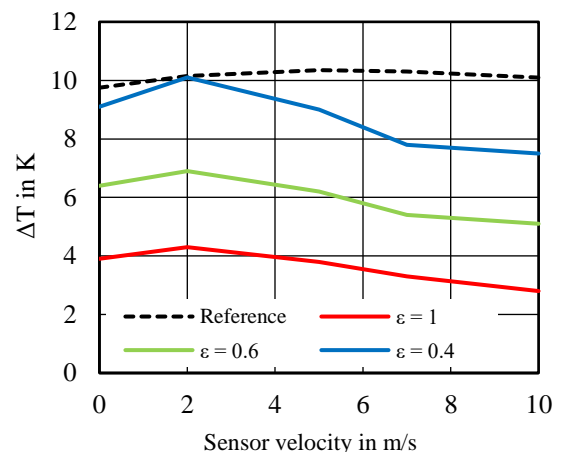

Figure 9. IR detected temperature differences between clamp and conductor for a distance of 30 m

So far, the experiments have shown, that measuring absolute temperatures in a dynamic environment accurately can be rather challenging. Nonetheless, it should be possible to detect potential failures or hot-spots by analyzing temperature differences which has proven to be feasible under dynamic conditions. Furthermore, the experiments have shown that results measured with a higher emission coefficient are less dependent on sensor velocity.

3. Performance of UV sensors in dynamic use

3.1 State-of-the-art

Corona discharges emit in air mainly in the 230 – 405 nm range of the UV [3]. Unfortunately, corona emissions are very weak in intensity in relation to solar UV irradiance. However, there is a so called "solar blind band" between 240 – 280 nm where the solar radiation is absorbed by the earth's ozone layer. Commercially available corona cameras operate within this window. Corona emission lines in this spectral band are weaker in intensity than in the 290 – 400 nm range. Therefore, corona cameras usually rely on UV solar blind image intensifiers to provide high contrast images [4]. Additionally, a solar blind band pass filter is used to block out any leakage UV radiation which might saturate the image amplifier system [5].

3.2 Assessment of corona images

The assessment of corona images is inherently difficult and has been a vast field of research for many years. The main difficulty originates from the image intensifier's high gain (typically 10^6 ph/ph) which causes all corona discharges to appear as bright white spots of similar size (blobs) against a black background (Figure 10).

Figure 10. Corona "blob" image recorded with UV camera

A single corona image does therefore not allow any assessment or classification regarding the intensity or severity of the corona inducing defect. However, in recent years, several methods for the classification of corona inducing defects have been developed. Those approaches usually rely on the extraction of features from a series of corona image frames with machine learning algorithms [6 – 9]. However, while all authors conclude that correlation is feasible for stationary setups with constant distances, it remains unclear whether those algorithms are still applicable for dynamic conditions and to what extent the detection of blobs is influenced by velocity and distance in general. To gain further experience in this respect, laboratory experiments were carried out under realistic dynamic conditions.

3.3 Testing environment

The corona UV experiments were carried out with a UV camera manufactured by ProxiVision equipped with an image intensifier and a solar blind filter (Table 4). The test object was a needle-plane-arrangement which produced continuous, branched discharges with an apparent charge of about $Q = 100$ pC. The distance between the camera and the test object was varied between 10 m and 40 m. To replicate dynamic operating conditions, the same turntable arrangement as described in chapter 2.3 was used. For every distance the velocity was varied in following steps: 5 m/s, 10 m/s and 15 m/s. The experiments were carried out with two different UV lenses with different focal lengths (25 mm and 60 mm, both F 2.8). Additionally, the influences of the camera's shutter speed on the detection sensitivity under dynamic conditions were investigated (20 ms, 40 ms and 60 ms).

Table 4. Technical details of the UV camera

| Photocathode	Extended Solar Blind
Microchannel plates	2, Chevron Configuration
Sensor	Sony ICX285
Resolution	1392 x 1040 Pixel
Frame rate	30 fps
Solar Blind Filter	$\lambda_C = 265$ nm, BW = 19 nm

3.4 Results

One of the main objectives of this work is to analyse the influence of various experimental variables, e.g. distance to target object, velocity of moving platform, camera exposure time, etc. onto the ability of detecting events captured by UV equipment. To this end, a set of relevant markers meant to describe this ability was defined, which were monitored across various sets of experimental conditions. Focusing on the UV case, a typical image produced by such a camera, has a resolution of 694×510 pixels. A *blob detection* algorithm, aiming to obtain the 2D location of all bright areas along with their corresponding sizes was applied to the recorded pictures. Typical blob detection algorithms are based on thresholding and filtering operations applied to the (grayscale) image.

The result of this algorithm is a set of blob detections. A 2D point is assumed to be in the same image plane that corresponds to the location of the physical UV event, which acts as ground truth (gt) information for the experiment.

A single recording sequence, as described in chapter 3.3, comprises a collection of such images augmented with detections and annotated gt information. In these conditions, the following statistical markers can be computed: *n1* – the percentage of frames from the sequence containing at least one detected blob, *n2* – the percentage of frames with *confirmed* gt, where a gt point is considered to be confirmed if there is at least one detection no further than a specified radius (r) from it, *n3* – the percentage of *flooded* frames, where a frame is labelled as flooded if the number of detected blobs exceeds a value of 10, and finally *n4* – the number of actual frames with confirmed gt in a session.

The above markers were compiled for a total of 72 condition sets, combinations of 4 from the following experimental variables: $d \in \{10,20,30,40\}$ – the distance (m) between the camera and the target object, $f \in \{25,60\}$ – the focal length (mm) of the camera optics, $e \in \{20,40,60\}$ – camera exposure time (ms) and $v \in \{5,10,15\}$ – equivalent velocity (m/s) of a point passing in front of the target on a linear trajectory at distance d and producing the same recording session (ignoring lens distortions). Throughout the experiment, the radius r for confirming a gt annotation point was set to 20 pixels.
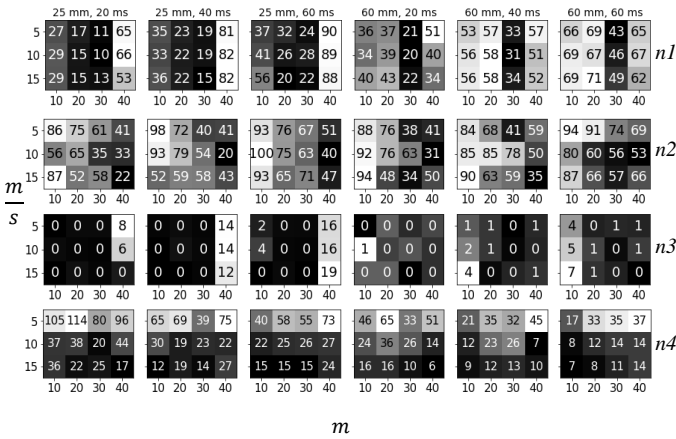
Figure 11. Statistical markers $n1$– $n4$ (rows 1 – 4 respectively) computed for various sets of experimental conditions
(d on x-axis and v on y-axis)

The following observations can be drawn from the results visible in Figure 11: marker $n3$, the percentage of flooded frames, is negligible, with few exceptions that affected experiments with the 25 mm lens at 40 m distance and the 60 mm lens at 10 m distance. These sessions (clustered in time) are likely to have been influenced by some external perturbation, or perhaps some technical problem of the UV camera. The abnormal percentage of flooded frames has a direct consequence on $n1$ (for the corresponding sessions), particularly visible for the 25 mm lens (row 1, columns 1-3). Otherwise, $n1$ seems to be influenced primarily by distance when using the 25 mm lens, which indicates a low percentage of detections as the distance to the test object increases. For the 60 mm lens, however $n1$ does not change much with distance (with the sole exception of $d = 30$ m). Distance has a similar influence on $n2$, where the negative correlation seems to be much clearer than that for $n1$. The percentage of confirmed defects ($n2$) decreases on average to approximately half, as distance increases from 10 m to 40 m. This observation is consistent across different focal lengths and exposure time values.

Velocity shows a clear negative correlation on $n4$. This correlation is to be expected, since as velocity increases, the number of frames with the defect in the field of view of the camera decreases (and this is the upper bound for $n4$). As will be mentioned in chapter 4, $n4$ has a clear significance when consolidating 2D detections, being the main parameter that decides the final form of the solution.

Exposure time appears to be positively correlated with $n1$ and $n2$, although this dependency is not as clear as for the distance. In general, a higher percentage of detections and a higher percentage of confirmed annotations can be observed as the exposure increases.

Finally, when deciding between different focal lengths, the experiments favour the higher f value, which gives an increased percentage of both detections and confirmed annotations.

In general, a high confirmation rate ($n2$ and $n4$) for most combinations of experimental factors can be observed, which supports the feasibility of automatic detection of UV events.

4. Case study: automatic detection of UV events using Computer Vision

Automatic detection of 2D blobs in UV images is very useful in localizing events such as corona defects, especially when the blobs can be linked temporally. In this chapter an example of temporal aggregation of blobs in 3D with the scope of highlighting UV events that are consistent across multiple frames is shown. To this end, an algorithm that takes as input blob detections from multiple frames and camera calibration information and produces aggregated 3D points that accumulate votes from individual frames was developed. The algorithm formulates the problem as a point search in 3D, constrained by elements of epipolar geometry and general camera geometry [10]. Blobs detected in one frame are projected in 3D as line segments bounded by a fixed depth of interest. Points from these segments are back-projected and matched (up to a matching tolerance) in consecutive frames. Consequently, vote counters are incremented for successfully confirmed blobs. Finally, the points accumulating a certain number of confirmations form the solution.

While the technical details of the algorithm are beyond the scope of this chapter, the outcome of applying it will be demonstrated on a semi-realistic scenario: detection and localization of a 3D point visible in multiple consecutive images. For ease of verification, the tip of a pylon cross-arm, whose 2D location is annotated in multiple consecutive frames forming a trajectory segment, will be considered. Figure 12 shows a sample image and the location of the considered point. The data comes from an inspection flight performing a high voltage overhead line monitoring routine and includes RGB (grayscale) and LIDAR data streams.
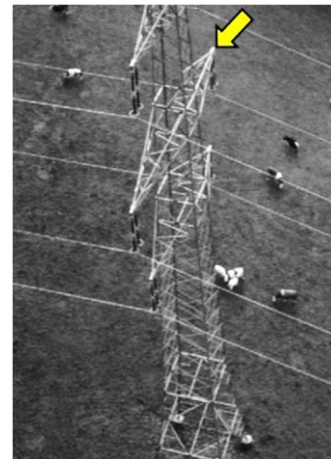
Figure 12. Reference point for the point aggregation algorithm

Next, a minimum number of 50 votes of a point from the solution was chosen for the algorithm. The value of this parameter is supported by Figure 11, for the case of 25 mm lens, a distance of approx. 40 m and a velocity between 5 and 10 m/s, reflecting the recording conditions. The outcome is printed in 3D in Figure 13, using 3D rendering software superimposed onto LIDAR data [11]. The number of votes each 3D point accumulates is encoded in shades of gray (with brighter shades corresponding to more votes). The red points mark the camera trajectory over time.


Figure 13. Outcome of the temporal aggregation algorithm on a semi-realistic scenario

The solution calculated with the algorithm can be further post-processed by applying a clustering algorithm exploiting the voting information. However, even in this unfiltered form the localization is fairly accurate, with neighboring points being approx. 30 cm apart from each other.

In order to quantify the quality of the localization, a second experiment was conducted, where the point with the highest number of votes from the above solution was considered (reference point) and then projected back onto all the frames from the trajectory segment.

Since corona discharges are recorded by an UV camera with a location uncertainty around the actual physical defect (e.g. sharp tip of a broken conductor), this uncertainty was modelled by adding Gaussian noise with increasing standard deviation to the projected locations of the reference point. As performance metric, the distance error between the reference point and the solution point with the highest number of votes was measured. Figure 14 shows the outcome of this experiment.
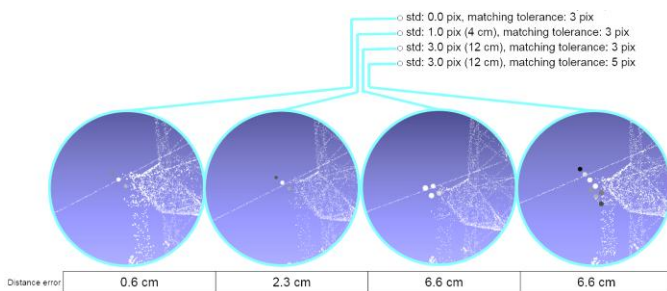
Figure 14. Simulation of the location uncertainty of UV corona discharges by adding Gaussian noise

As expected, increasing the noise level results in more validated points in the raw solution and also in an increase in the distance error.

Overall, a distance error of this magnitude is rather encouraging, and currently to be expect in realistic conditions.

5. Conclusion

The experiments with the IR camera have shown, that measuring absolute temperatures in a dynamic environment accurately can be rather challenging. Nonetheless, it should be possible to detect potential failures or hot-spots by analyzing temperature differences which has proven to be feasible under dynamic conditions. Furthermore, the experiments have shown that the emission factor is a crucial parameter for long distance thermography.

The measurements carried out with the UV camera clearly indicate that automatic optical corona detection is also possible under dynamic conditions. While different experimental conditions influence the quantity of redundant information used when consolidating 2D blob detection in 3D (e.g. see the impact of velocity on *n4*), a sufficiently large number of frames with confirmed ground truth (*n4*) appears to be ensured in most situations. This in turn makes automatic 3D localization of corona defects possible.

6. Acknowledgments

References

[1] S. Krüll and D. Henning, „Thermografie in Wartung und Instandhaltung", *Elektropraktiker*, EP 3, Berlin, 2010.

[2] Y. Hu and L. Kai, "Inspection and Monitoring Technologies of Transmission Lines with Remote Sensing", Beijing: Elsevier Inc., 2017.

[3] F. Grum and L. F. Costa, "Spectral Emission of Corona Discharges", *Applied Optics*, Vol. 15, No. 1, 1976, pp. 76-79.

[4] M. Lindner, S. Elstein, P. Lindner, J. M. Topaz and A. J. Philipps, "Daylight Corona Discharge Imager", *11th International Symposium on High Voltage Engineering*, Report 467, London, 1999, pp. 349-352.

[5] M. Lindner, S. Elstein and J. Wallace, "Solar Blind Bandpass Filters for UV Imaging Devices"*, Digital Solid State Cameras: Designs and Applications*, Vol. 3302, 1998, pp. 176-181.

[6] F. Lv, R. Dai, H. Li and H. Jin, "Comparison of Two UV Imaging Parameters in the Insulator Fault Diagnosis", *International Conference on Intelligent Systems Design and Engineering Application*, Sanya, 2012, pp. 1400-1403.

[7] C. P. G Guedes, E. G. Costa, G. L. Ribeiro and A. D. Germano, "Classification of the Degradation Condition of Polymeric Insulators by UV Radiation Levels (Corona) and Fuzzy Logic"*, 19th International Symposium on High Voltage Engineering*, Pilsen, 2015.

[8] W. Zhou, H. Li, X. Yi, J. Tu and J. Yu, "A Criterion for UV Detection of AC Corona Inception in a Rod-Plane Air Gap"*, IEEE Transactions on Dielectrics and Electrical Insulation*, Vol. 18, No. 1, 2011, pp. 232-237.

[9] J. Li, X. Yi, M. Zhang, X. Chen, M. Cui and F. Yan, "An Automatic Corona-Discharge Detection System for Railways Based on Solar-Blind Ultraviolet Detection"*, Current Optics and Photonics*, Vol. 1, No. 3, 2017, pp. 196-202.

[10] R. Hartley and A. Zisserman, "Multiple view geometry in computer vision", *Cambridge university press*, 2003.

[11] P. Cignoni, M. Callieri, M. Corsini, M. Dellepiane, F. Ganovelli and G. Ranzuglia, "MeshLab: an Open-Source Mesh Processing Tool", *Sixth Eurographics Italian Chapter Conference*, pp 129-136, 2008.